Proceedings of the ASME 2010 3rd Joint US-European Fluids Engineering Summer Meeting and 8th International Conference on Nanochannels, Microchannels, and Minichannels
FEDSM-ICNMM2010
August 1-5, 2010, Montreal, Canada

FEDSM-ICNMM2010-30033

ANALYSIS OF COMPLEX FLOWS FROM EXPERIMENTAL DATA AND NUMERICAL EXPERIMENTS

Jérôme Vétel*
Department of Mechanical Engineering
École Polytechnique de Montréal
Montréal, Québec, H3C 3A7
Canada
Email: jerome.vetel@polymtl.ca

André Garon
Email: andre.garon@polymtl.ca

Dominique Pelletier
Email: dominique.pelletier@polymtl.ca

ABSTRACT

Fluid mechanics is considered to be a privileged field in physics because phenomena can be made visible. This is unfortunately not the case in turbulence where diffusion and mixing of passive tracers are enhanced by turbulent transport. Consequently, the analysis of the rich flow physics provided by direct numerical simulations (DNS) and by modern optical diagnostic techniques require advanced post-processing tools to extract fine flow details. In this context, this paper reviews most recent techniques used to reveal coherent structures and their dynamics in turbulent flows. In particular, results obtained with standard Eulerian techniques are compared to those obtained from a more recent Lagrangian technique. Even if this latter technique can provide finer details, it is found that the two methods are complementary. This is illustrated with DNS results and with experimental data including planar measurements as well as time-resolved measurements converted to quasi-instantaneous volumetric data by using the Taylor hypothesis.

INTRODUCTION

Vortical structures, that form and develop in the early stages of turbulence, and coherent structures that appear in latter stages are difficult to capture experimentally due to their transient nature. The intermittency precludes for example the use of ensemble-averaging techniques and therefore measurements have to be performed simultaneously at different locations in space. Direct numerical simulations (DNS) have partially circumvented these experimental limitations and became a valuable tool to perform *numerical experiments* where most quantities are still challenging to measure. However, the analysis of such complex flows is often performed indirectly by the use of additional techniques that extract averaged flow properties thanks to sophisticated statistical tools.

The increasing capabilities of measurement techniques lead to a renewed interest in experimental sciences. In particular, while volumetric particle image velocimetry (PIV) is still in its infancy, currently available PIV systems can capture simultaneously large and small-scale vortical structures thanks to enlarged dynamic ranges and time-resolved measurements. This offers opportunities to reconstruct accurate quasi-instantaneous three-dimensional velocity vector fields using the Taylor hypothesis, and thus to compute all the components of the full velocity gradient tensor over a volume. The knowledge of fine flow details that result from these measurements allows to supplement DNS simulations whose results are highly sensitive to initial and boundary conditions for which clear information is still lacking.

This paper presents post-processing techniques that are used to extract flow structures and to understand the flow physics, with a particular emphasis on Eulerian and Lagrangian methods. This is illustrated through examples where both experimental and numerical aspects can be found in the literature, most of them being derived from turbulent boundary layers and internal flows.

*Address all correspondence to this author.

VORTEX IDENTIFICATION AND DETECTION TECHNIQUES

Vortex identification criteria

The identification of vortical structures is a long-standing problem and a vortex does not have a unique definition. Most vortex identification techniques are based on point-wise analysis of the velocity gradient tensor (Eulerian criteria). These techniques are routinely used to locate vortex cores and the now classical works of Hunt *et al.* [1] on the Q-criterion, Chong *et al.* [2] on the Δ-criterion, Jeong & Hussain [3] on the λ_2-criterion and Zhou *et al.* [4] on the λ_{ci}-criterion (the swirling strength criterion) are widely cited in the literature. Surprisingly, while Eulerian criteria were known to identify similar structures in most flows, their mathematical equivalences were clearly explained only recently in the work of Chakraborty *et al.* [5]. However, these definitions provide Galilean-invariant criteria which are not frame-independent as for example in the case of rotating frames. This led Haller [6] to propose an *objective* definition of a vortex, based on a Lagrangian method.

The Lyapunov exponent is widely used in dynamical system theories, but its finite-time counterpart was only introduced recently by Haller [7]. The approach is based on characterizing coherent structures in terms of the stretching of initially adjacent fluid particles. It was shown that the extraction of Lagrangian coherent structures (LCS) is able to provide a powerful tool to describe unsteady flows and represents an alternative to Eulerian criteria. Later, Shadden and coworkers [8] provided a theory which explained the mixing and transport properties of LCS, acting as material lines thus revealing the geometry of flow systems.

The computation of finite-time Lyapunov exponent (FTLE) involves the determination of particle trajectories over a time T which can be positive or negative. The Lagrangian nature of the method restricted the number of applications both by the inherent three-dimensional nature of the computation and its prohibitive computational cost (the work of Garth *et al.* [9] proposes an adaptive scheme to compute FTLE fields). Therefore, applications of the FTLE computation in turbulence are essentially found in direct numerical simulations, including two-dimensional turbulence [10] and fully turbulent channel flows [11], while experimental applications are limited to two dimensional flows [see 12] and two-dimensional turbulence generated in rotating water flows [13] (Koh *et al.* [14] presents results on the stratospheric polar vortex with the finite-*size* Lyapunov exponent).

In experiments, all these criteria can only be obtained from PIV results, since the PIV technique is the only method which provides accurate instantaneous velocity information in space, thus allowing the computation of the velocity gradient tensor. While the spatial resolution of PIV systems is near its optimum due to physical limitations [15], the temporal resolution is continuously increasing because of technology improvements in high-speed camera and high-repetition rate lasers. Therefore, better measurement capabilities lead PIV systems to capture the temporal behavior of a growing range of studies, which should increase the number of applications of the FTLE.

Furthermore, it would not be surprising that high-speed cameras become the standard in PIV in the near future. At present, this is not the case, owing to the smaller spatial resolution and signal-to-noise ratio generally achieved by CMOS cameras [16], which are the camera usually used for time-resolved measurements, compared with standard high-resolution CCD cameras. In turbulence, this is particularly critical, because measurements of small-scale velocity fluctuations are more sensitive to noise. However, in the case of the FTLE, the choice of using a high temporal resolution to the detriment of spatial accuracy may be justified. Since the Lagrangian criterion involves the computation of particle trajectories by temporal integrations, the method is naturally less sensitive to the noise than in the case of spacial differentiations, the latter being on the contrary extensively used by its Eulerian equivalents which are derived from the invariants of the instantaneous local velocity gradient tensor. This leads to reliable predictions, even in the case of large velocity errors [17].

Statistical detection approaches

To identify dominant eddies embedded in turbulent flows, statistical tools are generally used. Even if the proper orthogonal decomposition technique [18] is well-developed and despite their similarities [19], the stochastic estimation [20] is usually preferred, probably because it is more easy to implement. This estimation consists on using the conditional information at one or several locations in the flow to estimate the information at other locations by minimizing the error in a mean-square sense. This yields to a more simple flow model but in the same time reveals organized structures.

The linear stochastic estimation (LSE) technique is based on first order conditional averages of the velocity vectors, which is usually sufficient for qualitative estimates because higher-order terms generally show marginal improvement over linear estimation [21]. The procedure requires the calculation of the two-point second-order correlation tensor and involves the reconstruction of the conditional velocity field around the reference points. If only one reference is chosen, single-point conditional averages relate the size of the conditional structure to the integral scale of the flow. If a particular length scale has to be explored, multi-point procedures are used [22]. LSE can also include time dependence by computing the space-time correlation tensor.

The choice of the event vector that is used as the reference signal in the LSE depends on the nature of the eddies to be investigated. The reference point is placed at a location where the local velocity fluctuations are influenced by the convection of the vortex structure that is studied. The following section will investigate some results from the literature where different vortex pattern have been elucidated with this method.

Some numerical results

Zhou *et al.* [23] extracted the statistically most probable single structure from the DNS database of Kim *et al.* [24] on a low-Reynolds-number channel flow (the Reynolds number, based on friction velocity and channel half-width, is $Re_\tau = 180$). The reference point was placed at a wall-normal location of $y^+ = 49$ where a signature of a hairpin vortex can be captured, i.e. an ejection event vector in the second quadrant Q2 ($u' < 0$, $v' > 0$). The evolution of this initial vortex structure was then studied by superposing the hairpin-like vortical structure on a clean unidirectional turbulent flow. By this method, they visualized, with the λ_{ci}-criterion, the complex evolution of the initial vortex and revealed the phenomenon of autogeneration of new hairpin vortices by self- and mutual-induction as well as vortex reconnection processes, as illustrated in Fig. 1. This phenomenon is responsible for the generation of coherent packets of hairpin vortices.

The same initial hairpin vortex was also used by Green *et al.* [11] for testing of the FTLE method. Figure 2 presents two-dimensional cuts of the resulting Lagrangian criterion together with the structure visualized with the swirling strength criterion. Two-dimensional planes are used instead of iso-surfaces because the LCS are not constant value surfaces. While it is possible to obtain vortex frontiers by extracting FTLE ridges in three dimensions [9], visual inspection of two-dimensional cuts of the 3D field retain more details and is generally sufficient to interpret the LCS, except when the extraction of a particular LCS among other ones is desired for further analysis, as it can be the case in complex flows such as vascular flows [25]. In Fig. 2 for example, the three planes allow to provide fine details of the vortex signature. Results shown in Fig. 3 give a visualization of the flow at a later stage of evolution where a secondary hairpin is formed, which is the process preceding the formation of hairpin packets. Once again, the ability of the Lagrangian method to capture the whole structures is emphasized.

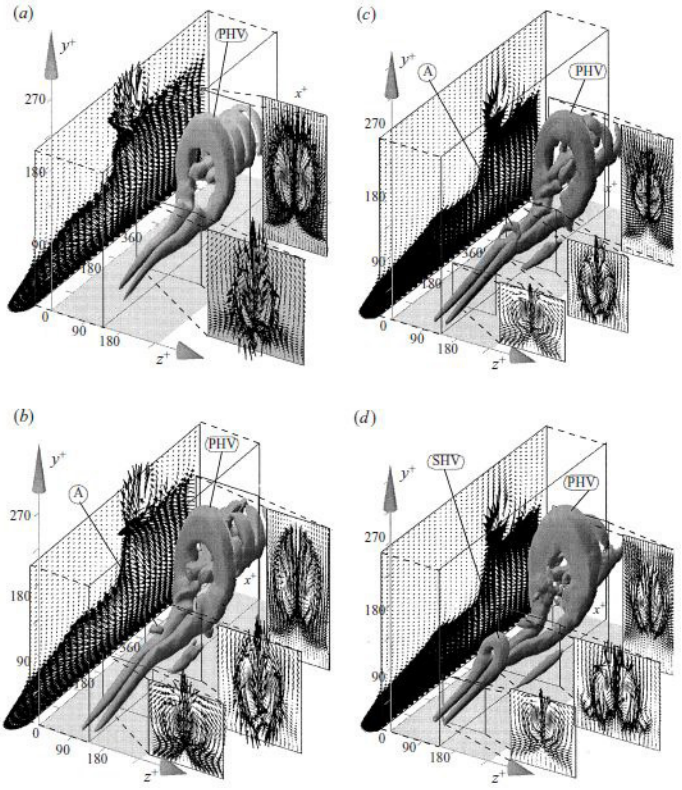

FIGURE 1. GENERATION OF A SECONDARY HAIRPIN VORTEX (SHV) FROM A SPANWISE VORTEX ARCH (A) FORMING ON THE PRIMARY HAIRPIN VORTEX (PHV); FROM [23].

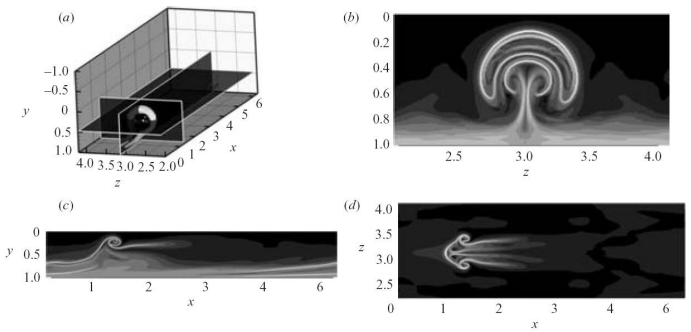

FIGURE 2. TWO-DIMENSIONAL CUTS OF THE 3D FTLE FIELD OF AN ISOLATED HAIRPIN VORTEX; FROM [11].

Further analysis of the authors showed that the birth of a secondary hairpin structure corresponds to a bifurcation along the LCS, captured by analyzing the hyperbolicity in the FTLE field. The evolution of the vortex pattern shown by the three time instants plotted in Fig. 4 clearly identifies the phenomenon. The Lagrangian criterion offers a way to recognize the formation and development of the second and subsequent hairpin structures. Compared to Zhou *et al.* [23], the finer details obtained with the FTLE by Green *et al.* allowed to detect the hairpin development earlier.

However, the event vector is a vortex marker that is not nec-

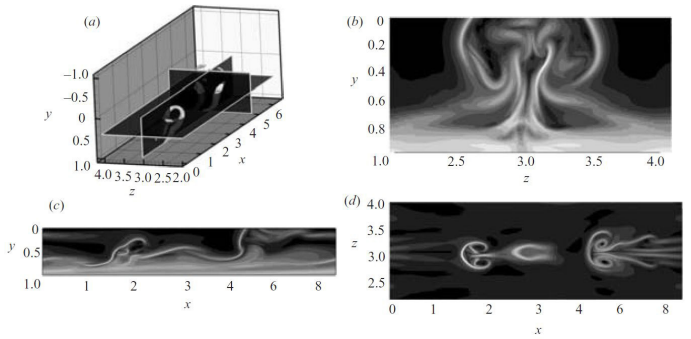

FIGURE 3. SAME AS IN FIG. 2 BUT AT A LATER STAGE OF EVOLUTION; FROM [11].

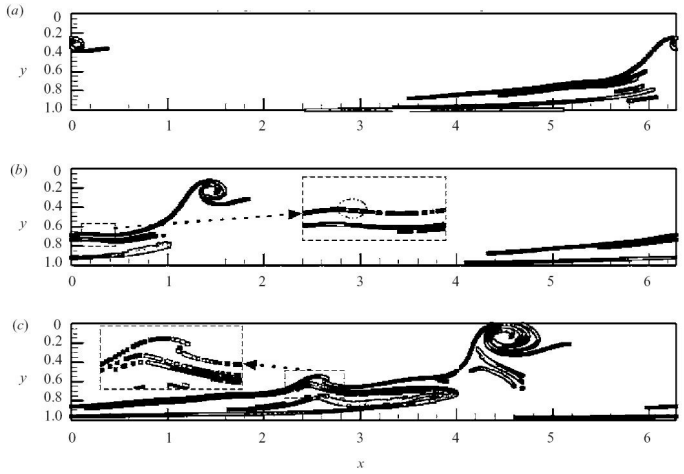

FIGURE 4. SECONDARY VORTEX FORMATION VISUALIZED BY THE RATE OF STRAIN NORMAL TO THE SURFACE OF THE LCS IN A SPANWISE CROSS-SECTION OF THE HAIRPIN VORTEX; FROM [11].

essarily a velocity fluctuation vector. For example, Christensen and Adrian [26] applied conditional estimations based on the swirling strength to the velocity structure in the outer region of a turbulent channel flow. The vortices identified by averages occur with sufficient strength to leave an imprint on the flow statistics, and consequently are an illustration of the dominant flow features. The pattern was consistent with observations of the outer-layer wall turbulence where groups of hairpin vortices are aligned in the streamwise direction.

Another interesting example can be found in the study by Tinney *et al.* [27]. Due to the differences in the spectral behavior between conditional and unconditional sources, an alternative approach, employing estimations based on cross-spectral relationships, is used. This spectral form of the LSE showed good accuracies of the estimated spectral quantities, emphasizing the direct impact of filtering incoherent correlations through the computation of coherence spectra.

These examples show that most physical aspects of vortex formation and development processes have been obtained from numerical computations. However, even if DNS databases represent invaluable information sources since they provide numerical experiments (as demonstrated again recently by Wu and Moin [28]), such simulations are sensitive to the prescription of the inflow and boundary conditions. For example, in simulations of homogeneous turbulence, most computations are performed in periodic cubes, taking advantage of the Fourier series in the streamwise direction. However, while the size of the cube L should be larger than the size of the biggest structures ℓ (the integral scale), in practice this is rarely achieved, except for low values of the Reynolds number. Consequently, if L is only a few multiples of ℓ, the periodicity imposed between the upstream and downstream faces of the cube leads to the presence of an artificial anisotropy and long-range correlations on scales $\sim L$ (see for example Davidson [29], chapter 7)

Even if DNS computations are now frequently used in most of research laboratories, the range of problems is considerably limited. In parallel, the increasing capabilities of measurement techniques has led to a renewed interest in experimental sciences. For example, standard high-performance PIV systems allow to capture large velocity vector fields in time, and could provide information that is still lacking to DNS simulations. In the next sections, we focus on experimental tools that contribute to provide such information, and we start with the interpretation of two-dimensional measurement data.

TWO-DIMENSIONAL EXPERIMENTAL DATA

The hairpin vortex paradigm proposed by Adrian and coworkers [32] allowed to describe the spatial organization and evolution of the hairpin coherent structures into streamwise-aligned packets (see Fig. 5), as the simulations of Wu and Moin seem to confirm [28]. This also revealed the prominent role of such structures in the development of boundary layers. It is interesting to see that this paradigm was evidenced in experiments only by two-dimensional flow inspections, including qualitative visualizations and quantitative two-component PIV measurements in streamwise-wall-normal planes. Figure 6 shows for example typical results obtained by Adrian and coworkers on the organization of hairpin packets, where long packets occur inside larger ones [30]. The color contours correspond to the swirling strength in the lower plot and to the spanwise vorticity in the upper, expanded plot. Since measurements are performed in a plane, the full local velocity gradient tensor cannot be obtained, so that a two-dimensional form of the λ_{ci}-criterion is used instead [33]. However, as observed in Figure 6, the criterion is localized in space at the vortex centers. In a population of vortices, characterized by a large range of wavelength, lumped in

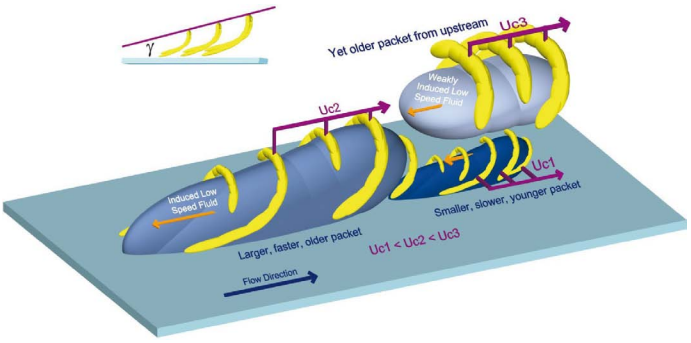

FIGURE 5. CONCEPTUAL SCENARIO OF THE ORGANIZATION OF HAIRPIN PACKETS IN A TURBULENT BOUNDARY LAYER; FROM [30].

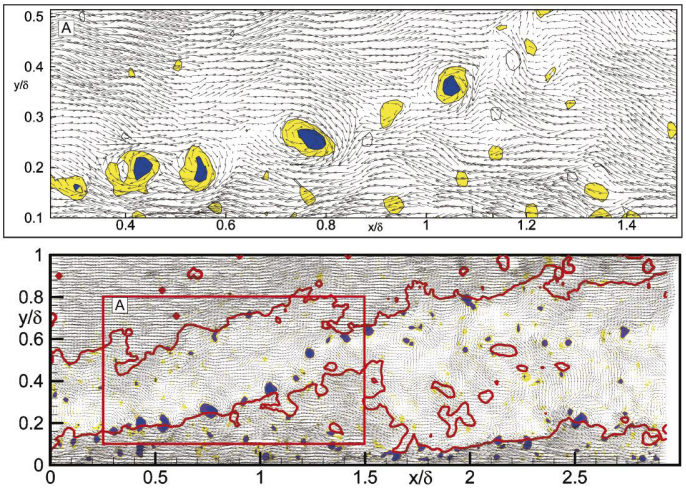

FIGURE 6. EXAMPLE OF HAIRPIN PACKETS COMMONLY OBSERVED IN EXPERIMENTS CONDUCTED BY ADRIAN AND COWORKERS; FROM [30].

a measurement noise, the interpretation of results is not always straightforward.

Another example is shown in Fig. 7 where the turbulent flow generated by the development of a jet issuing from a smooth constriction in a pipe is measured by PIV in a meridional plane [31]. This flow is extensively used in biomechanical studies to model stenoses in arteries. Both experimental [34] and numerical results [35] agree on the fact that critical Reynolds numbers, above which the flow becomes unstable, are low, which allows, in experiments, to describe the temporal evolution of the flow by using available acquisition frame rates of standard time-resolved PIV systems. Results presented in Fig. 7 were obtained for $Re \sim 1000$, where the Reynolds number Re is based on the parameters of the unrestricted pipe. Figure 7a presents an instantaneous velocity vector field in a frame of reference moving with the vortices while Fig. 7b shows contours of the resulting spanwise vorticity. The growth of the disturbances developing from the beginning of the jet results in the formation of structures which are alternately shed from the top and bottom shear layers. However, these shear layers are also revealed by both the velocity and the vorticity fields. In order to more precisely extract the vortical structures embedded in the background shear, Fig. 7c presents the fluctuating velocity vector field obtained from the Reynolds decomposition. While the development of the shear layers has been removed, the resulting vector field lacks clarity. Indeed, the Reynolds decomposition reveals more vortices than Galilean decompositions for small-scale vortices which travel at velocities often close to the local mean velocity [see 33]. Larger vortices, better revealed by the large uniform momentum regions associated to the mean flow, are masked by the Reynolds decomposition. Even if the λ_{ci} contours clearly identifies different structures (Fig. 7d), this two-dimensional equivalent of the swirling strength criterion cannot help to identify the nature, the form and the signature of each vortex because only their centers are revealed, while their connections are masked. On the contrary, in the case of hairpin-like vortices, the structure is more easily recognized by revealing the unsteady shear, as for example the local shear layers resulting from the upward flow pumping of quasi-streamwise vortices that forms the legs.

Figure 8 presents the Lyapunov exponent field computed with data of Fig. 7, where only attracting material lines are visualized. This means that the FTLE was computed by integrating trajectories backward in time ($T < 0$) to reveal vortical structures, since fluid particles collect in forward times towards the vortex centers. The top plot was obtained by using the initial PIV mesh grid. In the upper part of the flow, the birth of a first vortex is observed, followed by a spiraling pattern clearly indicating the rolling of a structure, which is very similar to that seen in the Kelvin-Helmholtz instability. A third structure is observed downstream, but is destabilized by the increasing irregularity of the flow. In the lower part of the flow, the flow is more irregular which emphasizes the asymmetry of the instantaneous flow at this instant. However, the FTLE seems blurred, due to the limited spatial resolution of the PIV grid. One advantage of the Lyapunov exponent is that the resolution can be improved by increasing the number of computed trajectories, i.e. by using in-

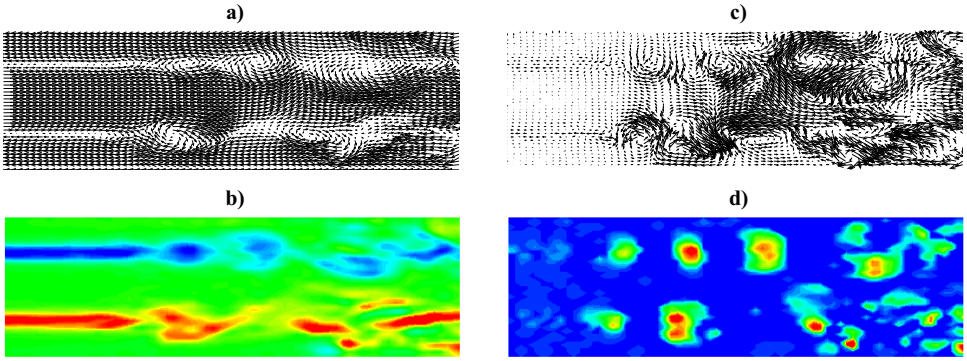

FIGURE 7. JET ISSUING FROM A SMOOTH CONSTRICTION IN A PIPE: (a) INSTANTANEOUS VELOCITY FIELD VIEWED IN A FRAME OF REFERENCE MOVING WITH THE VORTICES; (b) SPANWISE VORTICITY; (c) FLUCTUATING VELOCITY FIELD AND (d) λ_{ci} FIELD. THE FLOW IS FROM LEFT TO RIGHT; ADAPTED FROM [31].

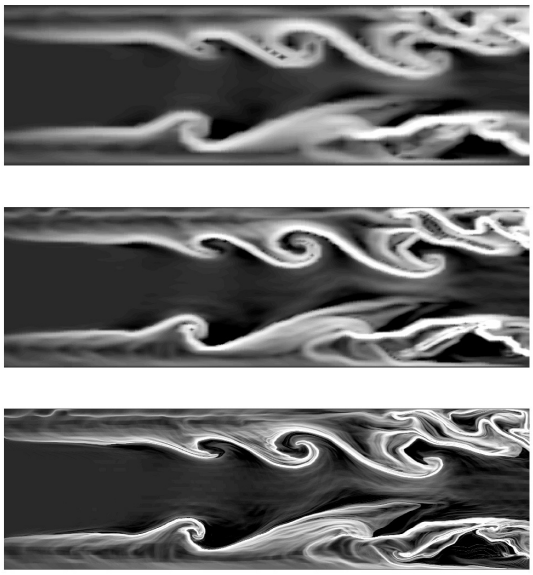

FIGURE 8. INSTANTANEOUS FTLE FIELDS COMPUTED WITH DATA OF FIG. 7 FOR DIFFERENT RESOLUTIONS; ADAPTED FROM [31].

terpolation to obtain a finer grid than the original velocity data. While this does not provide more information on small-scale vortices, this allows to increase the sharpness of large-scale vortices. The middle plot shows results obtained by dividing the initial resolution Δx and Δy by 2, then by 8 (bottom plot). This last plot allows to reveal more details on turbulent structures and the overall results clearly identifies the development and transition of the internal jet emanating from the constriction. This is remarkably similar to the flow details obtained from dye visualizations that are not revealed by more classical Eulerian techniques.

An example that better illustrates the effect of the resolution is shown in Fig. 9. Measurements were obtained in a flow cross-section where the development of two counter-rotating vortices is captured. The figure shows contours of the out-of-plane vorticity component and details of the in-plane velocity vector field in close-up views. In the top right boxed region, the interaction of the main vortex (left) with the wall led to the formation of a new spiraling pattern (right) with an opposite rotation sign. In the bottom left boxed region, a second vortex is observed. A line of opposite vorticity (yellow region) is also identified close to this structure but the velocity field reveals that this vortical region is more the result of the local shear rate, which coincides with a region of high momentum, rather than of a rotating structure. The other plots of Fig. 9 show the FTLE field obtained by computing the trajectories on the PIV grid for different resolutions. For this illustrative example, we assume that the flow is steady and the FTLE is computed using only one two-dimensional velocity vector field. The integration length T was chosen to best reveal the flow structure. For the original resolution Δx and Δy, the two main rotating patterns are highlighted by the spiraling form of the FTLE contours, where white levels indicate the highest values. Generally, more of the flow structure is revealed with longer integration times. This was not possible in the example of Fig. 8 because velocity data are limited in space, and therefore the number of fluid particles leaving the domain increases with T and some trajectories are lost in the computation of the FTLE. In Fig. 9, the rotating patterns that characterize the vortices should keep most trajectories inside the domain. However, for the same resolution and for a time interval of $2T$, the FTLE contour levels are more diffuse and the boundaries of vortices disappear. This effect is in fact due to the coarse initial PIV mesh. By decreasing the grid spacing, it is observed that greater details can be captured. As expected boundaries of vortices become sharper but do not change. In turn, this allows to compute the FTLE field with longer integration times. The last plot illustrates the result of a computation by dividing the initial resolution by a factor of 16

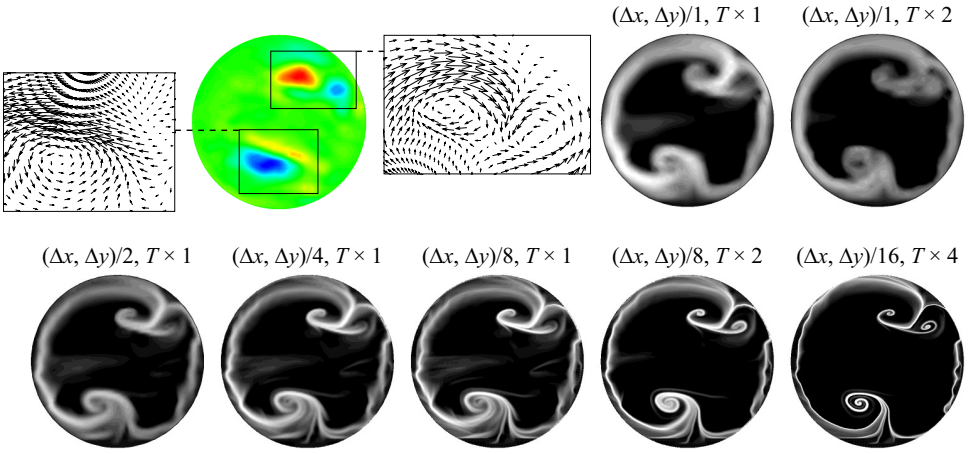

FIGURE 9. EXAMPLE OF FTLE COMPUTATION IN A CROSS-SECTION OF THE FLOW DEVELOPING DOWNSTREAM OF A CONSTRICTION IN A PIPE FOR DIFFERENT RESOLUTIONS AND INTEGRATION TIMES. DETAILS OF THE VELOCITY VECTOR FIELD ARE GIVEN WITH THE STREAMWISE VORTICITY; ADAPTED FROM [31].

and increasing the time interval to $4T$, i.e. four times the initial value. This last computation resolves more of the Lagrangian structure by presenting spiraling patterns particularly clear and sharp. In particular, while previous plots did not show the boundaries of the new vortex forming in the top right region, the double structure is now clearly identified. The value of the integration time and the spatial resolution are thus chosen depending on the amount of detail to show, since boundaries of the Lagrangian structures are not affected by the integration time.

The sequence of FTLE fields presented in Fig. 10 illustrates a temporal transition to turbulence downstream of the smooth constriction. The time step ΔT and the reference time t_0 correspond to a time scale and a time origin chosen to provide the best insights of the temporal flow evolution. For example, the beginning of the sequence is plotted every $20\Delta T$ to show the initial steady flow and the growth of the instability (note that vertical lines correspond to time lines, see [31]). At $t = t_4$, flow perturbations begin to appear, and spatial oscillations of the internal jet are observed in the subsequent frames. A weak structure appears at $t = t_9$ (see the white box) and at $t = t_{10}$ the general shape recalls the vortex signature of a hairpin vortex (see Fig. 2), which could indicate that the onset of instability is accompanied by the formation of hairpin-like structures before breakdown to turbulence. Progressively, flow perturbations occur more rapidly and as early as the upstream region of the flow. We can distinctly follow the formation of a structure between $t = t_{12}$ and $t = t_{19}$. At $t = t_{12}$ the vortex signature in the FTLE field appears only as an inclined straight line. However, in subsequent frames, the line is distorted and at $t = t_{16}$ a rolling process indicates the formation of a spanwise vorticity concentration. Again, until $t = t_{17}$, the temporal process is similar to the phenomenon shown in Fig. 4. When the vortex is formed, a lift up process occurs and is particularly clear in frames t_{18} and t_{19}. This specific phenomenon is similar to the generation of coherent packets of hairpin vortices described by Zhou *et al.* [23] (see Fig. 1). A mutual induction process induces the breaking of the two quasi-streamwise vortex legs of a primary hairpin vortex. The upstream sections of the legs then connect with a bridge of spanwise vorticity to form a secondary hairpin vortex. The heads of the newly formed vortices then lift-up and evolve into Ω-shaped vortices, and can reach almost a vertical orientation. By examining results shown in Fig. 10, this is especially clear between $t = t_{12}$ and $t = t_{19}$. Finally, the vortex formation mechanism repeats itself between $t = t_{18}$ and $t = t_{21}$ where a new structure forms. The last frames

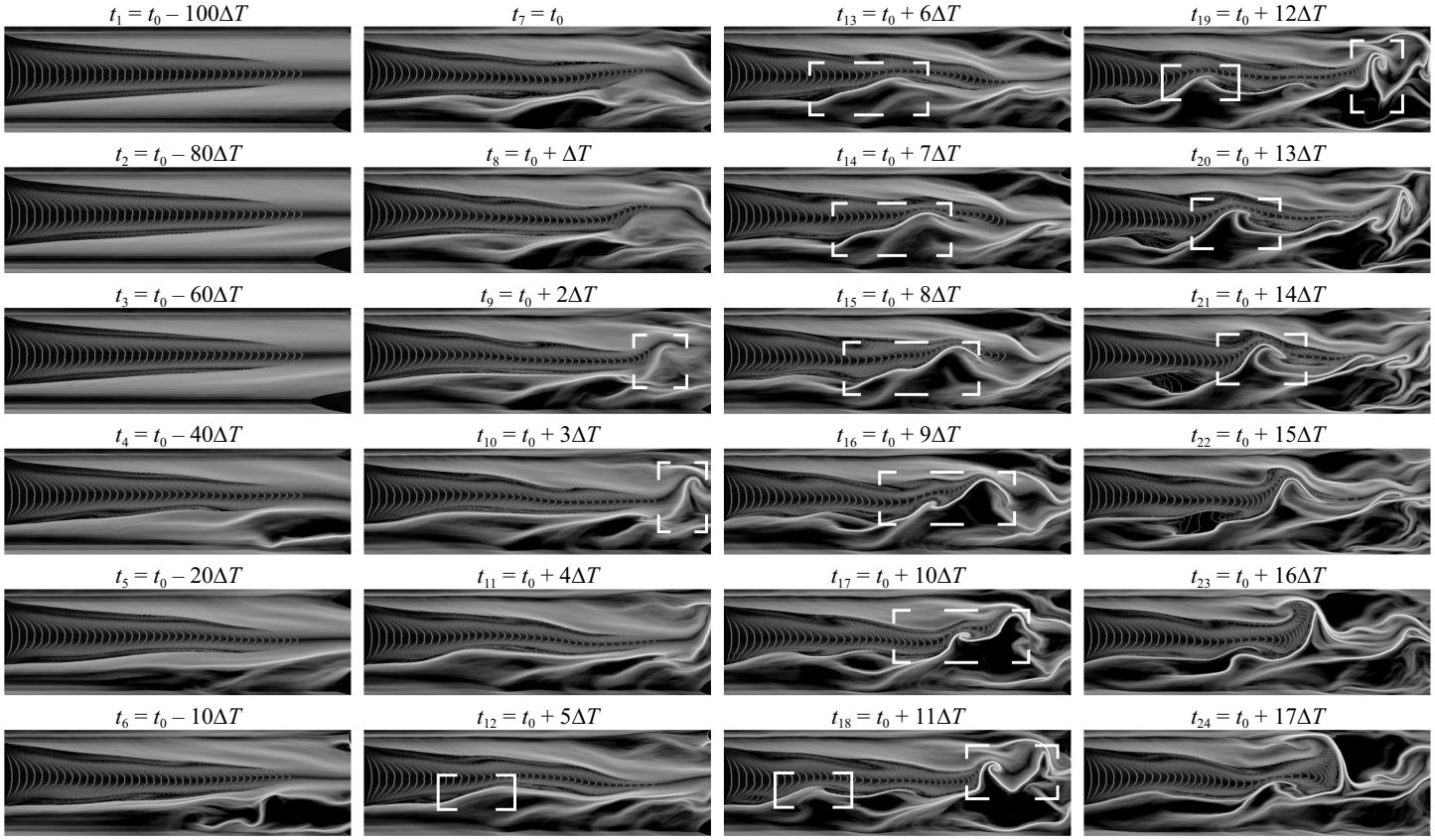

FIGURE 10. EXAMPLE OF EVOLUTION WITH TIME OF FTLE FIELDS; FROM [31].

show that the flow perturbations increase with time and indicate the transition of the flow towards a more perturbed state and possibly turbulence.

Even if these results are of valuable interest, they are only qualitative since fluid particle trajectories are computed in two dimensions whereas they are three-dimensional. Some techniques can however be used to obtain information in the third direction.

THREE-DIMENSIONAL EXPERIMENTAL DATA

With the incoming of volumetric/tomographic PIV systems [36], the measurement of the three components of velocity vectors in volumes (3D3C) is now possible [37–40], and in a few cases, data are also resolved in time [41,42]. However, the implementation of such systems requires more attention than standard PIV systems and is still restricted to a small range of applications. Therefore, 3D3C systems will not be investigated here. Instead, we will focus on volumetric data that can be reconstructed from planar PIV measurements.

Steady flows

Steady flows are the simplest examples where the three-dimensional velocity vector fields can be reconstructed since the volumetric data can be obtained from measurements that do not need to be acquired simultaneously. Only one example is given here and is provided by the authors [see 43]. The problem concerns the complex steady flow developing in a model of the human carotid artery bifurcation. In the geometry shown in Fig. 11, the bifurcation stems from the common artery dividing into two asymmetric branches, the internal and external arteries (relative to their progression inside or outside the skull). Near the bifurcation, the common carotid widens to form the carotid sinus which maintains adequate blood pressure thanks to its baroreceptors. The division of flow into the daughter branches varies with time during the cardiac cycle resulting in an average over the cycle of approximately 30%/70% (external/internal).

To study hemodynamics phenomena, a transparent negative of the carotid artery was build [see 44] to make it possible to use stereoscopic PIV techniques. To illustrate the flow complexity, Fig. 12 (left) shows iso-surfaces of the axial velocity for a positive and a negative value together with characteristic streamlines for two flow divisions. For a flow division of 30%/70%, i.e. for the mean physiological conditions, a reversed flow region is located in the side of the external artery. The trajectory shown indicates that the back flow is in fact the result of a complicated helical path of the streamline. The iso-surface of positive velocity for this flow repartition shows no secondary motions, in particular in the internal artery. Instead, the fluid flows naturally in the geometry which seems optimized to direct the blood through the daughter vessels with a specific flow division. These results

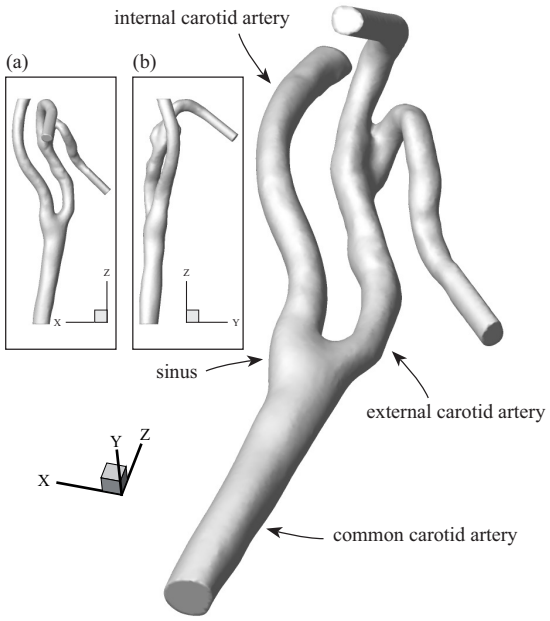

FIGURE 11. EXAMPLE OF A CAROTID ARTERY BIFURCATION GEOMETRY. (a) TOP VIEW, (b) SIDE VIEW; FROM [43].

agree with previous investigations [45] where flow visualizations showed the presence of complex three-dimensional zones with flow reversal and helices, however not identified as recirculation regions since fluid was not entrapped inside.

In the case of a chronic disease, the flow division can be modified. For example, atherosclerosis may result in artery wall remodeling and narrowing, and in most severe cases, this leads to the formation of a stenosis in the sinus region inducing a major flow restriction. Results obtained for a flow division of 50%/50% is shown in Fig. 12 (right). For the streamline shown, the initial fluid particle location is chosen close to the upper wall of the carotid model. The particle follows the main artery and moves initially towards the internal artery. As it approaches the

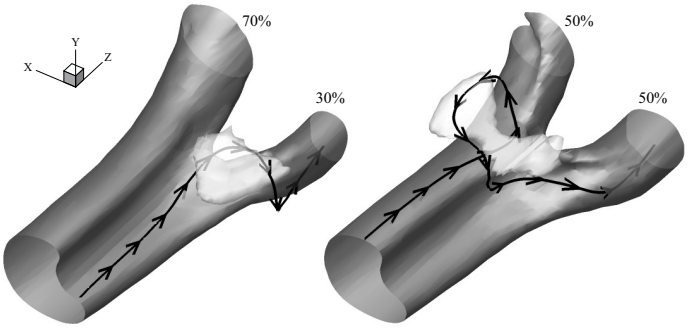

FIGURE 12. ISO-SURFACES OF A POSITIVE (DARK) AND A NEGATIVE (CLEAR) AXIAL VELOCITY VALUE WITH CHARACTERISTIC STREAMLINES; FROM [43].

bifurcation, the particle takes an upstream direction, crosses the common artery transversally and finally enters into the external artery. Therefore, this flow distribution indicates that the flow can reach a higher degree of complexity for non-physiological conditions. In particular, a recirculation region could be identified contrary to the previous case.

To confirm the presence of a recirculation region for a flow division of 50%/50%, the 3D FTLE field was computed with the full measurement data set. Results are illustrated in Fig. 13. The figure presents the FTLE field by characteristic two-dimensional cuts in the axial and transverse directions together with the location of the planes in the model (high values correspond to black contours). In slice (1), the spiraling pattern occurring in the right daughter branch is particularly well represented, which confirms the presence of helical trajectories in this region. A closed region is also clearly identified in the top left corner of slice (1). Until now, negative values of the FTLE field have been used, since steady or unsteady vortical structures have been investigated, as seen previously. The FTLE can also be computed in forward time ($T > 0$), and resulting structures are called repelling material lines since the FTLE ridges indicate stretching of trajectories [8]. Therefore, the FTLE field computed in forward time can be used to detect reattachment surfaces, since particles initially located on either side of the surface move away from each other, while on the contrary the FTLE field computed in backward time can be used to detect separation surfaces. Since the two methods yield complementary information, they can be conjointly used to reveal complex flow structures, such as 3D recirculation regions which are difficult to extract.

For example, the FTLE computed with $T < 0$ and shown in slice (1) in Fig. 13 is also presented with $T > 0$. It allows to reveal two distinct regions. Further, the presence of a recirculation region is confirmed since the boundary of the top left region appears in backward and forward time computations, which is not the case of the spiraling structure. The constant-x cut plotted in slice (2) computed for $T > 0$ provides a view of the recirculation region showing the spatial extent in the axial direction. Slice (3) is another cut in the axial direction but at a location downstream of the bifurcation. While in the external artery the structure of the FTLE is difficult to describe, a clear spiraling pattern is observed in the left artery. This suggests that downstream of the recirculation region, fluid particles which were not entrained by the reverse flow follow a helical path as they move downstream. This result is confirmed by the flow representation proposed by Bharadvaj *et al.* [45,46].

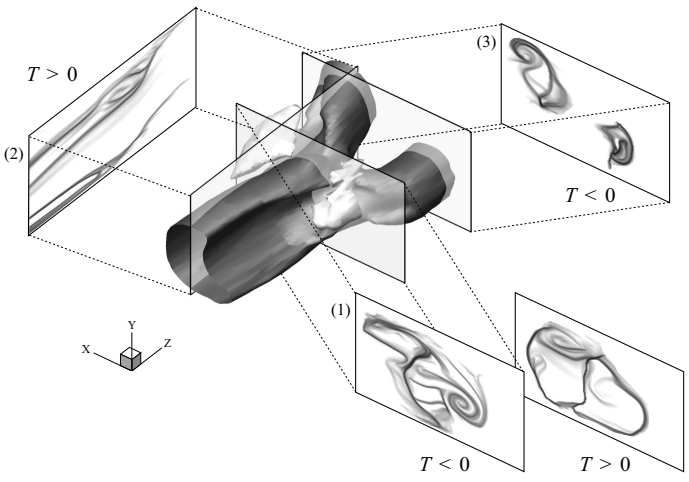

FIGURE 13. 2D CUTS OF THE 3D FTLE FIELD WITH ISOSURFACES OF A POSITIVE (DARK) AND A NEGATIVE (CLEAR) AXIAL VELOCITY VALUE; FROM [43].

For heart failure patients under maximal ventricular assist device (continuous flow pump) support, the flow rate within the systemic circulation is constant. In this case, the flow division between the daughter vessels may be different from the physiological mean values. Therefore, these results show that the complex flow structure that could appear as a consequence of an abnormal flow division may be a source of further blood damage due to an increase of residence time of red blood cells in the bifurcation area. To completely assess the extent of these problematic regions, further analysis would be necessary to extract ridges of the Lagrangian coherent structures in three dimensions, as was performed by Shadden and Taylor [25] from numerical simulation data in a carotid artery bifurcation flow.

In the following section, the more general case of unsteady flows will be investigated.

The Taylor hypothesis for unsteady flows

To highlight the spatial structure of unsteady flows, an approximate three-dimensional method of vortex identification can be applied. Stereoscopic PIV measurements obtained in flow cross-sections, i.e. in planes normal to the main flow direction, provide the three velocity components: two in-plane and one out-of-plane. To estimate data in the streamwise direction, the Taylor hypothesis can be used. The time-history of the flow as seen from a fixed reference frame can be interpreted as the advection of a frozen spatial structure traveling with the convection velocity u_c, so that the time is replaced by a spatial coordinate, i.e. $\mathbf{u}(z,t) = \mathbf{u}(z - u_c t, 0)$.

Spatial derivatives relative to the in-plane coordinates in cross-sections can be obtained by central difference approximations and derivatives relative to the axial direction are estimated with the Taylor hypothesis by using the relation $\partial_z = -u_c^{-1}\partial_t$. The sampling frequency has therefore to be high enough to obtain accurate time signals to evaluate time derivatives, and this requires also an estimate of the convection velocity u_c. Zaman and Hussain [49] showed that, in turbulent shear flows, the Taylor hypothesis yields acceptable results only if a constant convection velocity is used over the entire flow field. On the contrary,

Ganapathisubramani *et al.* [50] showed by direct comparisons that the use of a convective velocity equal to the local mean velocity also yields good results for reconstructing volumetric data from cinematographic stereoscopic PIV measurements in a turbulent round jet. However, the authors focused on the measurement of the fine-scale structure of turbulence, which justifies the use of a local convection velocity.

In the case of large-scale structures, the hypothesis of a constant advection velocity u_c is generally adopted, as in the work of van Doorne and Westerweel [51] where the bulk velocity in a pipe flow experiment is taken as the reference velocity. They observed numerous streamwise vortices that reveal the internal organization of the flow. A visualization of the vortical structures that they obtained is for example shown in Fig. 14. A quasi-periodic formation of hairpin-like vortices is clearly observed which allowed to show that such structures play a crucial role in the late stages of the transition to turbulence.

In the work of Matsuda and Sakakibara [48], u_c was deduced from cross-correlation measurements and used to reconstruct, with the Taylor hypothesis, the turbulent vortical structures that develop in the far-field region of a round free jet. As evidenced in Fig. 15, a group of hairpin-like vortices is observed to develop at the frontiers of the jet.

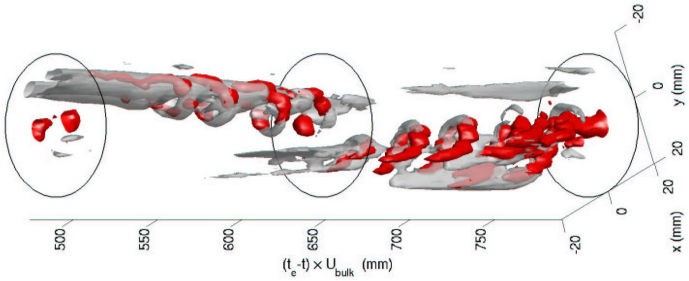

FIGURE 14. VISUALIZATION OF VORTICES IN A PIPE BY ISO-SURFACES OF THE Q-CRITERION (RED) AND THE IN-PLANE STREAMWISE VORTICITY (GRAY); FROM [47].

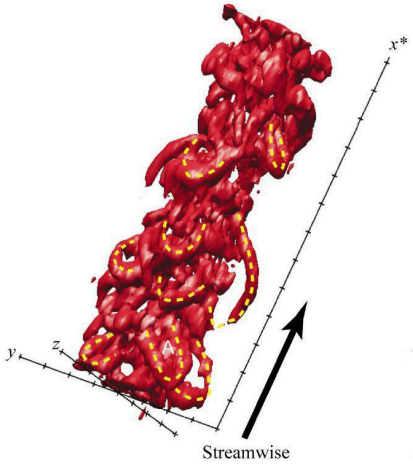

FIGURE 15. VISUALIZATION OF VORTICES IN A FREE JET BY ISO-SURFACES OF THE λ_{ci}-CRITERION; FROM [48].

A similar procedure was used by Vétel *et al.* [34] to compute the convection velocity in the flow downstream of the constriction. Two-component, time-resolved PIV measurements were acquired in a meridional plane and the two-point correlation function was estimated between a fixed reference signal and a moving probe both located on the axis of the pipe. A first example is illustrated in Fig. 16. The perspective view in Fig. 16a shows a typical vortical structure identified with the λ_{ci}-criterion. The arch of the vortex, essentially composed of spanwise vorticity, and the neck form a Ω-shape head connected to a pair of counter-rotating quasi-streamwise vortices forming long legs trailing behind, typical of a hairpin-like vortex. The velocity vector field obtained in the symmetry plane [34] confirmed strong similarities with 2D signatures of hairpin vortices available in the literature, as in Fig. 1 and in [26]. These results finally confirm that the phenomenon described in Fig. 10 occurred from the evolution of hairpin-like vortices, as previously inferred from numerical simulations.

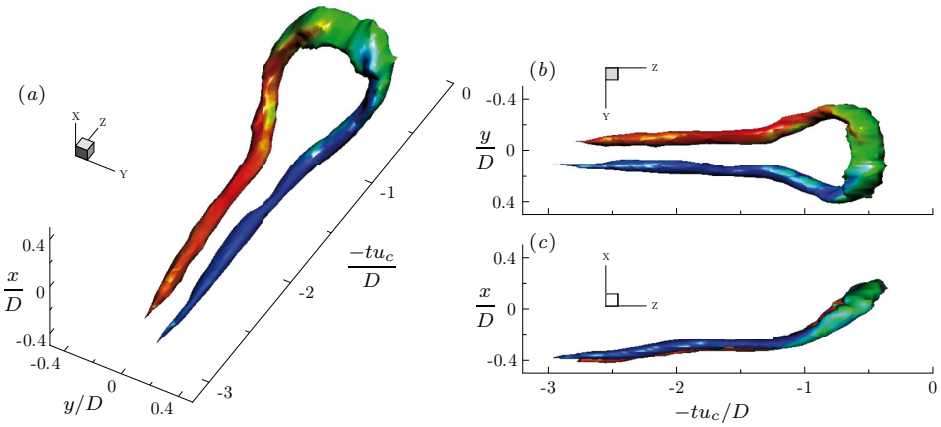

FIGURE 16. VORTICAL STRUCTURE EXTRACTED FROM THE FLOW DOWNSTREAM OF THE CONSTRICTION, VISUALIZED WITH THE λ_{ci}-CRITERION AND COLORED BY THE STREAMWISE VORTICITY; ADAPTED FROM [34].

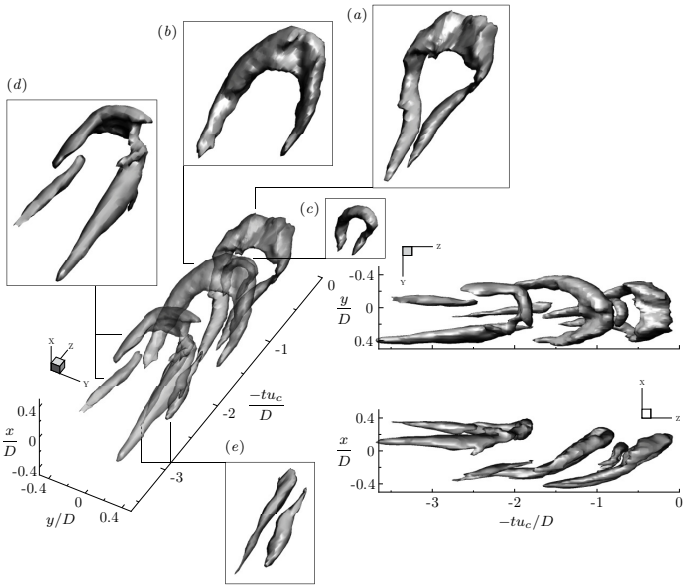

FIGURE 17. ANOTHER EXAMPLE OF VORTEX STRUCTURES EXTRACTED FROM THE FLOW DOWNSTREAM OF THE CONSTRICTION; FROM [34].

A second example of flow pattern is presented in Fig. 17. The perspective view shows several vortical structures rendered as translucent iso-surfaces of λ_{ci} whose value has been varied to achieve the best visualization for each vortex. The exploded view highlights the rich flow features. The structure in Fig. 17a is a Ω-shaped vortex and in Fig. 17b the pattern is close to a horseshoe vortex. Between these two structures, in Fig. 17c is a small Ω-shaped vortex. Adrian *et al.* [30] refer to all of these vortices by the unique terminology of hairpin-like structure, which can represent deformed versions of a common basic structure at different stages of evolution. Figures 17a–c illustrate the variety of sizes whereas the cane-vortex of Fig. 17d shows a different shape induced by the degree of asymmetry. Finally, the presence of a pair of counter-rotating quasi-streamwise vortices is shown in Fig. 17e.

Mixed methods

This last section gives examples where the different methods presented in this paper are jointly used. In the case of the smooth constriction [34], the LSE technique was applied on stereoscopic PIV measurements to identify the dominant flow eddies in the statistically stationary flow regime and to provide a basis for physical interpretation. The LSE included time dependence by computing the space-time correlation tensor based on the three velocity components recorded at a fixed streamwise location. The reference point was chosen in a radial coordinate close to a position of highest velocity fluctuation amplitudes, and results were found to be quite insensitive to the event vector. Finally, since the conditional averages were estimated in space and time, the Taylor hypothesis was used in a manner similar to that previously explained.

Results are shown in Fig. 18. In Fig. 18a, selected vorticity iso-surfaces corresponding to half the maximum are almost entirely composed of azimuthal vorticity and reflect the shear layer development downstream of the constriction. Identification of the vortices is performed in Fig. 18b by the λ_{ci}-criterion, which clearly demonstrates the predominance of vortex rings in the flow. Three complete patterns are entirely described which highlights the high degree of coherence of the structures identified, which are therefore dominated by vortex rings.

A 3D FTLE field was also computed from these volumetric flow data. Since this computation need to estimate fluid particle trajectories, the frozen pattern was simply advected in the streamwise direction at the convection velocity used to apply the Taylor hypothesis. A 2D FTLE field, obtained from a cut of the full 3D FTLE field, is shown in Fig. 18c. The three vortex rings are clearly identified by the presence of sharp boundaries delimiting six elliptical patterns from the main flow. By observing the orientation of the connections between these structures, it is possible to deduce their sense of rotation. The degree of flow details is particularly evident in the central core of each structure which exhibits a clear spiraling pattern illustrating the collection of fluid particles in the vortex center (light gray).

A similar procedure was applied on original velocity data (i.e. without LSE statistics) measured with different flow conditions. Figure 19 shows a Ω-shaped vortex identified by the λ_{ci}-criterion, and 2D FTLE fields extracted in the vertical plane of symmetry and in a horizontal plane. In the symmetry plane, the structure is distinctly observed with sharp boundaries upstream and downstream of the vortex core. The general shape is quite similar to that of a wave, and the fluid particle movements indicate that the rotation of the vortex core is clock-wise in this

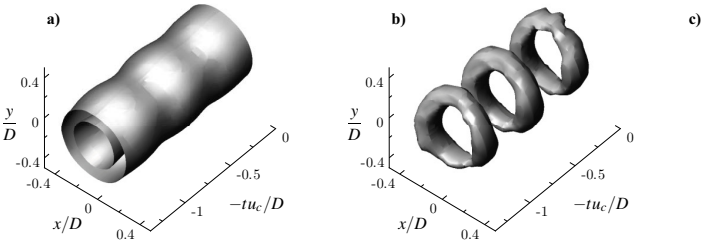

FIGURE 18. TAYLOR HYPOTHESIS APPLIED TO LSE DATA IN THE FLOW THROUGH THE CONSTRICTION: a) ISO-SURFACES OF VORTICITY, b) ISO-SURFACE OF λ_{ci} AND c) 2D CUT AT $y/D = 0$ OF THE 3D FTLE FIELD; ADAPTED FROM [31, 34].

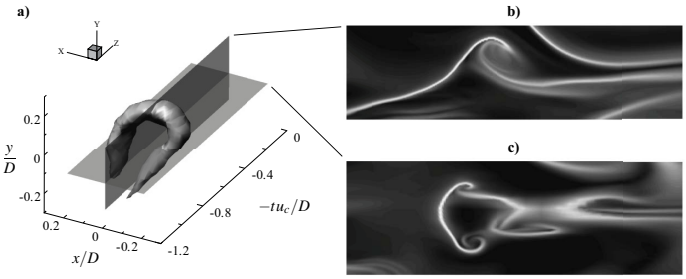

FIGURE 19. VORTEX STRUCTURE EXTRACTED FROM THE FLOW THROUGH THE CONSTRICTION REVEALED BY THE λ_{ci} AND THE FTLE CRITERIA; FROM [31].

plane. This is confirmed by the two counter-rotating spiraling patterns, generated by the vortex legs, observed in the horizontal plane. More details are difficult to obtain even if the integration time or the resolution are increased. Indeed, the strength of the Lagrangian approach is that, by essence, the Lyapunov exponent is determined by the history of the velocity field. By using the Taylor hypothesis and advecting the resulting structure in time, the flow is frozen. This implies that, on one hand, the large-scale mechanisms, which are responsible for the highest mean particle separations, are underestimated, and, on the other hand, the small-scale mechanisms, which are responsible for the randomness of the particle distribution in the flow field, are smoothed out. As a consequence, the use of a constant convection velocity with the Taylor hypothesis limits the study to the analysis of large-scale coherent structures, which reflects the lack of small-scale details in the FTLE fields.

However, results shown in Fig. 19 present similar features to the FTLE fields computed by Green *et al.* [11] and shown in Figs. 2 and 3. Since in their numerical simulation the isolated hairpin vortex was obtained with LSE to identify the statistically most probable flow field, small-scale velocity fluctuations was filtered by the procedure. This explains the close agreements with experimental results. This confirms that the method can yield sufficient information to obtain 2D FTLE signatures of hairpin-like vortices from a full 3D computation and therefore that they can be used as a vortex recognition technique.

CONCLUSION

This paper has reviewed some of the most popular techniques that are presently used to extract statistics on vortical structures as well as their identification in unsteady and turbulent flows. Applications of Eulerian and Lagrangian techniques to visualize structures revealed by linear stochastic estimation are particularly widespread in direct numerical simulations. While in such simulations the temporal behavior is naturally captured, this requirement limits experimental approaches to moderate Reynolds numbers. A considerable number of examples has therefore been derived from the flow developing through a constriction in a tube since the transition to turbulence is observed at low Reynolds numbers. With the use of the Taylor hypothesis on stereoscopic velocity data obtained in planes normal to the main flow direction, three-dimensional structures can be described. By performing the computation of the finite-time Lyapunov exponent, the signature of these structures can be obtained which allows to identify them in velocity data acquired in meridional planes with only two dimensions. For these latter measurements, further analysis can be conducted. Indeed, the use of the Taylor hypothesis is limited since the hypothesis of a frozen flow is not compatible with vortex interactions. These mechanisms were particularly well captured by using the Lagrangian criterion which can be computed on a finer grid than the original velocity data. Resulting phenomena were again similar to that obtained by direct numerical simulation studies found in the literature.

However, eventhough the recently developed Lagrangian methods are able to capture a large amount of flow details, and may even appear superior to the Eulerian methods, both techniques complement each other. Indeed, while the Lyapunov exponent method provides detailed 2D vortex signatures, the analysis of the 3D scalar field is complex and often requires to compute additional quantities to interpret the FTLE volume data. Therefore, Eulerian methods provide the vortex skeletons needed to analyze Lagrangian coherent structures.

It is finally interesting to note that as the hairpin-like structure and the general process of vortex packet formation are found to play a key role in boundary layers, during transition, in the near-wall and in the outer turbulent regions, they are also observed during the transition to turbulence in internal jet flows at Reynolds numbers as small as a few hundreds. Therefore the hairpin vortex paradigm appears as a unifying concept for transitional and turbulent wall bounded flows.

REFERENCES

[1] Hunt, J. C. R., Wray, A. A., and Moin, P., 1988. Eddies, stream, and convergence zones in turbulent flows. Tech. Rep. CTR-S88, Center for Turbulence Research.

[2] Chong, M. S., Perry, A. E., and Cantwell, B. J., 1990. "A general classification of three-dimensional flow fields". *Phys. Fluids,* ***2***, pp. 765–777.

[3] Jeong, J., and Hussain, F., 1995. "On the identification of a vortex". *J. Fluid Mech.,* ***285***, pp. 69–94.

[4] Zhou, J., Adrian, R. J., and Balachandar, S., 1996. "Autogeneration of near wall vortical structure in channel flow". *Phys. Fluids,* ***8***, pp. 288–291.

[5] Chakraborty, P., Balachandar, S., and Adrian, R. J., 2005. "On the relationship between local vortex identification schemes". *J. Fluid Mech.,* ***535***, pp. 189–214.

[6] Haller, G., 2005. "An objective definition of a vortex". *J. Fluid Mech.,* ***525***, pp. 1–26.

[7] Haller, G., 2001. "Distinguished material surfaces and coherent structures in three-dimensional fluid flows". *Physica D,* ***149***, pp. 248–277.

[8] Shadden, S. C., Lekien, F., and Marsden, J. E., 2005. "Definition and properties of Lagrangian coherent structures from finite-time Lyapunov exponents in two-dimensional aperiodic flows". *Physica D,* ***212***, pp. 271–304.

[9] Garth, C., Gerhardt, F., Tricoche, X., and Hagen, H., 2007. "Efficient computation and visualization of coherent structures in fluid flow applications". *IEEE T. Vis. Comput. Gr.,* ***13***, pp. 1464–1471.

[10] Lapeyre, G., 2002. "Characterization of finite-time Lyapunov exponents and vectors in two-dimensional turbulence". *Chaos,* ***12***, pp. 688–698.

[11] Green, M. A., Rowley, C. W., and Haller, G., 2007. "Detection of lagrangian coherent structures in three-dimensional turbulence". *J. Fluid Mech.,* ***572***, pp. 111–120.

[12] Voth, G. A., Haller, G., and Gollub, J. P., 2002. "Experimental measurements of stretching fields in fluid mixing". *Phys. Rev. Lett.,* ***88***(25), p. 254501.

[13] Mathur, M., Haller, G., Peacock, T., Ruppert-Felsot, J. E., and Swinney, H. L., 2007. "Uncovering the Lagrangian skeleton of turbulence". *Phys. Rev. Lett.,* ***98***(14), p. 144502.

[14] Koh, T.-Y., and Legras, B., 2002. "Hyperbolic lines and the stratospheric polar vortex". *Chaos,* ***12***, pp. 382–394.

[15] Adrian, R. J., 2005. "Twenty years of particle image velocimetry". *Exp. Fluids,* ***39***, pp. 159–169.

[16] Falchi, M., and Romano, G., 2009. "Evaluation of the performance of high-speed PIV compared to standard PIV in a turbulent jet". *Exp. Fluids,* ***47***, pp. 509–526.

[17] Haller, G., 2002. "Lagrangian coherent structures from approximate velocity data". *Phys. Fluids,* ***14***, pp. 1851–1861.

[18] Berkooz, G., Holmes, P., and Lumley, J. L., 1993. "The proper orthogonal decomposition in the analysis of turbulent flows". *Annu. Rev. Fluid Mech.,* ***25***(1), pp. 539–575.

[19] Bonnet, J. P., Cole, D. R., Delville, J., Glauser, M. N., and Ukeiley, L. S., 1994. "Stochastic estimation and proper orthogonal decomposition: complementary techniques for identifying structure". *Exp. Fluids,* ***17***(5), pp. 307–14.

[20] Adrian, R. J., and Moin, P., 1988. "Stochastic estimation of organized turbulent structure: homogeneous shear flow". *J. Fluid Mech.,* ***190***, pp. 531–559.

[21] Tung, T. C., and Adrian, R. J., 1980. "Higher-order estimates of conditional eddies in isotropic turbulence". *Phys. Fluids,* ***23***(7), pp. 1469–70.

[22] Guezennec, Y. G., 1989. "Stochastic estimation of coherent structures in turbulent boundary layers". *Phys. Fluids A,* ***1***(6), pp. 1054–60.

[23] Zhou, J., Adrian, R. J., Balachandar, S., and Kendall, T. M., 1999. "Mechanisms for generating coherent packets of hairpin vortices in channel flow". *J. Fluid Mech.,* ***387***, pp. 353–396.

[24] Kim, J., Moin, P., and Moser, R. D., 1987. "Turbulent statistics in fully developed channel flow at low Reynolds number". *J. Fluid Mech.,* ***177***, pp. 133–166.

[25] Shadden, S. C., and Taylor, C. A., 2008. "Characterization of coherent structures in the cardiovascular system". *Ann. Biomed. Eng.,* ***36***, pp. 1152–1162.

[26] Christensen, K. T., and Adrian, R. J., 2001. "Statistical evidence of hairpin vortex packets in wall turbulence". *J. Fluid Mech.,* ***431***, pp. 433–443.

[27] Tinney, C. E., Coiffet, F., Delville, J., Hall, A. M., Jordan, P., and Glauser, M. N., 2006. "On spectral linear stochastic estimation". *Exp. Fluids,* ***41***(5), pp. 763–775.

[28] Wu, X., and Moin, P., 2009. "Direct numerical simulation of turbulence in a nominally zero-pressure-gradient flat-plate boundary layer". *J. Fluid Mech.,* ***630***, pp. 5–41.

[29] Davidson, P. A., 2004. *Turbulence: An Introduction for Scientists and Engineers*. Oxford University Press.

[30] Adrian, R. J., Meinhart, C. D., and Tomkins, C. D., 2000. "Vortex organization in the outer region of the turbulent boundary layer". *J. Fluid Mech.,* ***422***, pp. 1–54.

[31] Vétel, J., Garon, A., and Pelletier, D., 2010. "Vortex identification methods based on temporal signal-processing of time-resolved PIV data". *Exp. Fluids,* ***48***(3), pp. 441–459.

[32] Adrian, R. J., 2007. "Hairpin vortex organization in wall turbulence". *Phys. Fluids,* ***19***(4), p. 041301.

[33] Adrian, R. J., Christensen, K. T., and Liu, Z.-C., 2000. "Analysis and interpretation of instantaneous turbulent velocity fields". *Exp. Fluids,* ***29***(3), pp. 275–290.

[34] Vétel, J., Garon, A., Pelletier, D., and Farinas, M.-I., 2008. "Asymmetry and transition to turbulence in a smooth axisymmetric constriction". *J. Fluid Mech.,* ***607***, pp. 351–386.

[35] Sherwin, S. J., and Blackburn, H. M., 2005. "Three-dimensional instabilities and transition of steady and pulsatile axisymmetric stenotic flows". *J. Fluid Mech.,* ***533***, pp. 297–327.

[36] Elsinga, G. E., Scarano, F., Wieneke, B., and van Oudheusden, B. W., 2006. "Tomographic particle image velocimetry". *Exp. Fluids,* ***41***(6), pp. 933–47.

[37] Hain, R., Kähler, C., and Michaelis, D., 2008. "Tomographic and time resolved PIV measurements on a finite cylinder mounted on a flat plate". *Exp. Fluids,* ***45***(4), pp. 715–24.

[38] Haigermoser, C., Scarano, F., and Onorato, M., 2009. "Investigation of the flow in a circular cavity using stereo and tomographic particle image velocimetry". *Exp. Fluids,* ***46***(3), pp. 517–526.

[39] Sharp, K. V., Hill, D., Troolin, D., Walters, G., and Lai, W., 2010. "Volumetric three-component velocimetry measure-

ments of the turbulent flow around a Rushton turbine". *Exp. Fluids,* ***48***(1), pp. 167–183.

[40] Troolin, D. R., and Longmire, E. K., 2010. "Volumetric velocity measurements of vortex rings from inclined exits". *Exp. Fluids,* ***48***(3), pp. 409–420.

[41] Schröder, A., Geisler, R., Elsinga, G. E., Scarano, F., and Dierksheide, U., 2008. "Investigation of a turbulent spot and a tripped turbulent boundary layer flow using time-resolved tomographic PIV". *Exp. Fluids,* ***44***(2), pp. 305–16.

[42] Burgmann, S., Dannemann, J., and Schröder, W., 2008. "Time-resolved and volumetric PIV measurements of a transitional separation bubble on an SD7003 airfoil". *Exp. Fluids,* ***44***(4), pp. 609–22.

[43] Vétel, J., Garon, A., and Pelletier, D., 2009. "Lagrangian coherent structures in the human carotid artery bifurcation". *Exp. Fluids,* ***46***(6), pp. 1067–1079.

[44] Hopkins, L. M., Kelly, J. T., Wexler, A. S., and Prasad, A. K., 2000. "Particle image velocimetry measurements in complex geometries". *Exp. Fluids,* ***29***, pp. 91–95.

[45] Bharadvaj, B. K., Mabon, R. F., and Giddens, D. P., 1982. "Steady flow in a model of the human carotid bifurcation. Part I–Flow visualization". *J. Biomech.,* ***15***, pp. 349–362.

[46] Bharadvaj, B. K., Mabon, R. F., and Giddens, D. P., 1982. "Steady flow in a model of the human carotid bifurcation. Part II–Laser-Doppler anemometer measurements". *J. Biomech.,* ***15***, pp. 363–378.

[47] van Doorne, C. W. H., 2004. "Stereoscopic PIV on transition in pipe flow". PhD thesis, Delft University of Technology.

[48] Matsuda, T., and Sakakibara, J., 2005. "On the vortical structure in a round jet". *Phys. Fluids,* ***17-025106***, pp. 1–11.

[49] Zaman, K. B. M. Q., and Hussain, A. K. M. F., 1981. "Taylor hypothesis and large-scale coherent structures". *J. Fluid Mech.,* ***112***, pp. 379–396.

[50] Ganapathisubramani, B., Lakshminarasimhan, K., and Clemens, N. T., 2007. "Determination of complete velocity gradient tensor by using cinematographic stereoscopic PIV in a turbulent jet". *Exp. Fluids,* ***42***, pp. 923–939.

[51] van Doorne, C. W. H., and Westerweel, J., 2007. "Measurement of laminar, transitional and turbulent pipe flow using Stereoscpic-PIV". *Exp. Fluids,* ***42***, pp. 259–272.